CrystEngComm

ROYAL SOCIETY OF CHEMISTRY

HIGHLIGHT

View Article Online
View Journal | View Issue

Cite this: *CrystEngComm*, 2025, **27**, 2611

Thiazolothiazole based functional metal–organic frameworks

Xing-Cai Huang * and Jiao-Jiao Kong*

Thiazolothiazole (TTZ)-based functional metal–organic frameworks (MOFs) represent an emerging class of materials that offer multi-functional properties, making them ideal for advanced applications in environmental monitoring, biomedical diagnostics, and sustainable technologies. Importantly, the distinctive structural features of TTZ ligands, characterized by two rigidly fused thiazole rings containing nitrogen and sulfur heteroatoms, provide exceptional fluorescence properties and multiple coordination sites, enabling diverse functionalities. Consequently, TTZ-based MOFs exhibit remarkable multifunctional characteristics attributed to the unique properties of the TTZ moiety, including fluorescence sensing, catalysis, photon upconversion, photochromism, electrochromism, bioimaging, and other functionalities. This comprehensive review systematically examines ligand design principles, synthetic methodologies, and diverse applications of TTZ-based MOFs. Furthermore, we critically analyze the current challenges and provide perspectives on future research directions in this field. The development of TTZ-based MOFs offers a promising strategy and alternative approach for addressing specific scientific and technological challenges in various research domains.

Received 15th February 2025,
Accepted 5th March 2025

DOI: 10.1039/d5ce00169b

rsc.li/crystengcomm

Introduction

Metal–organic frameworks (MOFs) are synthesized through coordination bonds between metal ions or clusters and a range of organic ligands.[1,2] These structures are utilized in various applications due to their exceptional properties, including ultra-high specific surface area, high porosity, and tunable porous architecture. The structure and properties of metal–organic frameworks (MOFs) are significantly influenced by various factors, including the functional groups, shape, and size of the ligands, as well as the type and number of coordinating atoms, such as carboxylate and N-heterocyclic ligands. By carefully selecting and designing organic ligands, MOFs can be tailored to exhibit diverse structural configurations and physicochemical properties. This versatility allows for fine-tuning of their

School of Chemistry and Environmental Engineering, Yancheng Teachers University, Yancheng, 224007, China. E-mail: huangxc82@126.com, huangxc@yctu.edu.cn, jiaokong0704@126.com

Xing-Cai Huang

Xing-Cai Huang is an associate professor of Chemistry and Environmental Engineering at Yancheng Teachers University. He obtained his PhD in Chemistry from Nanjing University in 2014. His research interests focus on fluorescence functional materials and molecular magnetic materials.

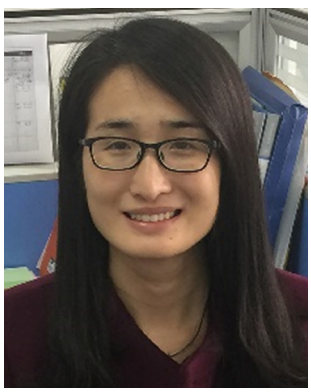

Jiao-Jiao Kong

Jiao-Jiao Kong is an associate professor of Chemistry and Environmental Engineering at Yancheng Teachers University. She obtained her PhD in Environmental Engineering from Shandong University in 2016. Her research interests focus on environmental functional materials.

porosity, stability, and catalytic activity, making them highly adaptable for applications in gas storage and separation,[3] sensing,[4,5] catalysis,[6] anticounterfeiting and security,[7] drug delivery,[8] and so on.

Thiazolo[5,4-*d*]thiazole, commonly referred to as thiazolothiazole (TTZ), which is a bicyclic [5–5] system with four heteroatoms [2 : 2], consists of two rigidly fused thiazole rings and exhibits a π-coplanar structure incorporating nitrogen and sulfur heteroatoms. First synthesized by Ephraim in 1891,[9] its correct structure was not conclusively determined until 1960 by Johnson.[10] Early research on TTZ derivatives was predominantly focused on their biological activity. However, recent investigations have broadened to explore their diverse properties, particularly their applications in covalent organic framework materials (COFs),[11–20] semiconductor materials,[21,22] organic solar cells,[23–26] organic light-emitting diodes (OLEDs),[27,28] fluorescent probes and sensors[29–33] and so on.

The thiazolo[5,4-*d*]thiazole (TTZ) group offers several advantageous properties,[34–36] including: (i) enhanced charge-carrier mobility due to its rigid planar backbone and extended π-conjugated electronic structure; (ii) high oxidative stability; (iii) stabilized downshifted energy levels in the solid state; and (iv) strong and broad absorption and fluorescence in the visible region, attributed to the rigid planar backbone and intense π–π stacking interactions. These characteristics make the TTZ scaffold highly valuable in the design and application of advanced functional materials.

The synthesis of TTZ derivatives predominantly relies on the Ephraim condensation reaction, a one-step process involving the condensation of dithiooxamide (rubeanic acid) with aromatic aldehydes. While the reaction can proceed without a solvent when using liquid aromatic aldehydes, the yield is often suboptimal. In contrast, the use of solvents such as DMF,[37,38] nitrobenzene,[39] or *n*-propanol[40] is recommended for solid aromatic aldehydes to improve reaction efficiency and yield.

Given the unique properties of TTZ and its derivatives, their integration into MOFs offers a promising avenue for constructing multifunctional materials with tailored properties. This review highlights the design principles, synthetic strategies, and diverse applications of TTZ-based MOFs, while also addressing current challenges and future directions in this rapidly evolving field. The development of TTZ-based MOFs not only expands the toolkit for material design but also provides innovative solutions to address specific scientific and technological challenges across multiple disciplines (Scheme 1).

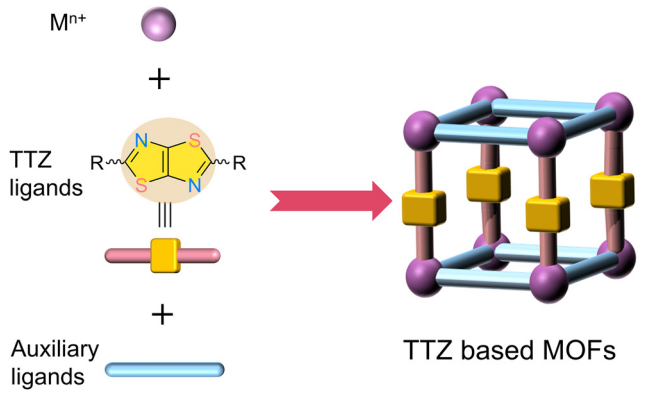

Scheme 1 The construction of thiazolothiazole based MOFs.

Construction of thiazolothiazole ligands and thiazolothiazole based MOFs

The creation of thiazolo[5,4-*d*]thiazole(TTZ) ligands primarily focuses on ligand design, which currently falls into two main categories: TTZ-based pyridine and TTZ-based carboxylic acid. TTZ-type pyridines can be easily synthesized in one step and possess two nitrogen-containing aromatic rings, exhibiting favorable optoelectronic properties. This makes them particularly valuable in the development of TTZ-based MOFs. Furthermore, the diversity of structures and properties in TTZ-based MOFs stems from the capacity to alter substituents on the bipyridine structure. This enables the fine-tuning of electronic properties and chemical environments, leading to enhancing performance in specific applications. Similarly, TTZ-type carboxylic acids contain functional groups that facilitate strong interactions with metal centers through deprotonation or chelation mechanisms. These ligands play a crucial role in stabilizing metal centers in complexes used for various catalytic and sensing applications. Their acidic nature also allows for effective participation in hydrogen bonding with other molecules or surfaces, along with π–π stacking, and C–H···π interactions inherent to the TTZ framework. Both classes have distinct characteristics that enhance their effectiveness as ligands in TTZ-based MOFs, making them promising building blocks for the construction of multifunctional materials.

To construct a synthetic TTZ ligand, modifications and decorations need to be made on the TTZ connecting groups. Extending the TTZ chromophore, particularly by incorporating additional aromatic rings, is a highly effective strategy for broadening the conjugation pathway. This modification can alter the interactions between intermolecular and intramolecular groups within TTZ, thereby changing the regions of UV-visible and fluorescence spectra of the TTZ ligands and enhancing or modifying their optical and electrical properties. This is particularly crucial for the design and development of new materials for advanced technologies.

Recently, three approaches for synthesizing MOFs using TTZ ligands have emerged. (1) Ketcham's method for one-step synthesis of TTZ pyridine[39] or TTZ carboxylic acid ester:[41] this method involves reacting nitrogen-containing aromatic aldehydes, such as pyridine or imidazole, or carboxylic acid ester-containing aromatic aldehydes with dithiooxamide. The nitrogen-containing aromatic aldehydes or carboxylic acid ester -based aromatic aldehydes can be synthesized using Pd-catalysed Suzuki or Stille cross-coupling reactions. (2) Ketcham's method for halogenated precursor

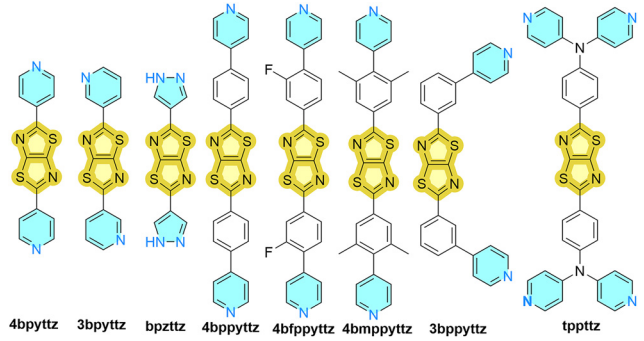

Fig. 1 The reported bipyridine-based TTZ ligands for TTZ-based MOFs.

synthesis and coupling reaction:[42] alternatively, TTZ pyridine or TTZ carboxylic acid precursors can be initially prepared by reacting halogenated aromatic aldehydes (*e.g.*, Br, Cl) with dithiooxamide, followed by Pd-catalyzed cross-coupling reactions to obtain TTZ pyridine or TTZ carboxylic acid. (3) Expansion of TTZ pyridine to obtain TTZ-based viologen-like carboxylic acids:[43,44] additionally, TTZ pyridine can be utilized to synthesize extended TTZ-based viologen-like carboxylic acids through further reactions. These three approaches provide efficient and versatile methods for synthesizing a wide range of TTZ-based ligands, expanding their potential applications in various fields.

Creating TTZ-based MOFs, much like other MOF materials, is achieved through solvothermal synthesis, utilizing several well-established ligand synthesis strategies. For bipyridine-based TTZ ligands (Fig. 1), a mixed ligand approach that combines bipyridine and multicarboxylic acid ligands is employed to construct MOFs with metal salts. The multicarboxylic acids used in this method are typically classified into binary, ternary, and quaternary carboxylic acids (Fig. 2). In the case of TTZ-based multicarboxylic acid ligands (Fig. 3), the most common method involves direct synthesis with metal salts. Similarly, TTZ viologen-type multicarboxylic acid ligands are also synthesized directly with metal salts *via* solvothermal methods. Additionally, TTZ viologen-type multicarboxylic acid ligands can be combined with auxiliary multicarboxylic acid ligands and bipyridine ligands through solvothermal synthesis to construct TTZ-based MOFs, enhancing their structural and functional properties.

Masciocchi and co-workers pioneered the use of thiazolo[5,4-*d*]thiazole-2,5-dicarboxylic acid (H_2TTZ) in MOFs.[45] While the Ag(I) derivative, $[Ag_2(TTZ)]_n$, formed a dense 3D framework *via* μ_6-bridging carboxylates and monodentate N-donor sites, first-row transition metal complexes (Mn, Co, Zn, Cu) adopted 1D polymeric chains. Unlike porous carboxylate-based frameworks, $[TTZ]^{2-}$ preferentially adopted NO-chelating over O,O′-bridging modes, suppressing porosity. Structural rigidity and S···S interactions in $H_2TTZ{\cdot}2H_2O$ suggested potential electronic properties.

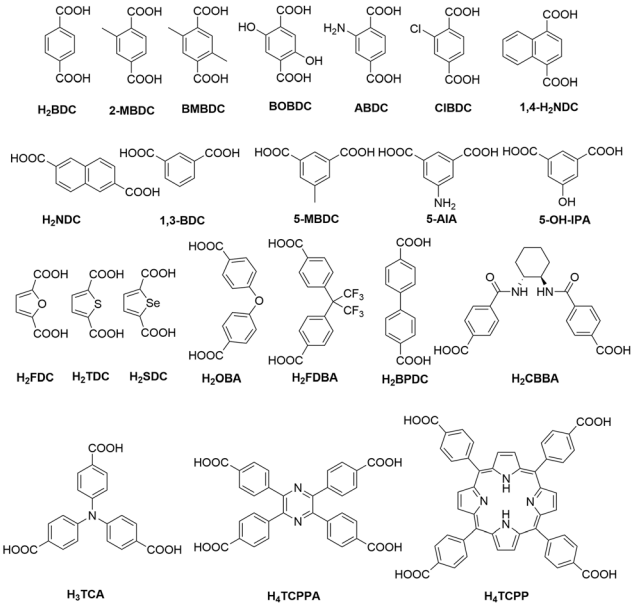

Fig. 2 The reported auxiliary multicarboxylic acid ligands in TTZ-based MOFs.

Chemical sensing

The fluorescence properties of MOFs are highly sensitive to their structural characteristics, coordination environment, pore surface properties, and interactions with guest species through coordination bonds, π–π interactions, and hydrogen bonds. These factors not only affect the luminescence intensity of MOFs but also determine their emission wavelength and lifetime, directly impacting the sensitivity and selectivity of sensors (Table 1).

Sensing metal ions

The contamination of water sources with toxic metal ions such as Hg^{2+}, Pb^{2+}, Fe^{3+}, and Cr(VI) is a growing concern attributed to industrialization and urbanization. Even trace levels of these ions can adversely affect human health and disrupt ecosystems. Bioaccumulation of these contaminants

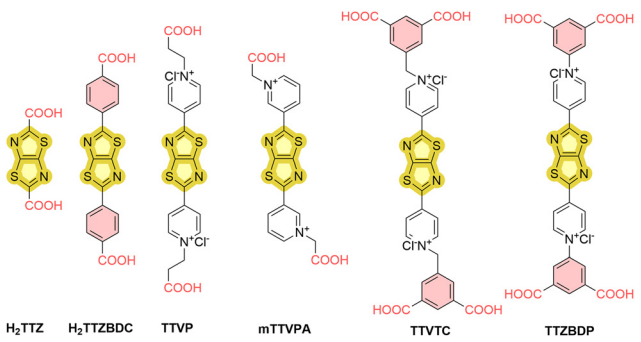

Fig. 3 The TTZ-based multicarboxylic acid ligands for TTZ-based MOFs.

Table 1 The reported TTZ-based MOF chemical sensors

MOF	Analyte	K_{sv} M^{-1}	LOD	Ref.
$[Zn_2(NDC)_2(4bpyttz)]_n$	Hg^{2+}	—	—	46
$\{[Zn(TTVTC)]\cdot 4H_2O\}_n$	CrO_4^{2-}	1.85×10^4	0.31 μM	43
	$Cr_2O_7^{2-}$	1.38×10^4	0.41 μM	
$\{\{Ag_4(4bpyttz)_4[Ag(PMo_{12}O_{40})_2]\}\cdot Ag(4bpyttz)\cdot 2(4bpyttz)\cdot 6H_2O\}_n$	Hg^{2+}	—	—	47
$[Zn(4bpyttz)(5\text{-}OH\text{-}IPA)]_n$	Hg^{2+}	8.43×10^4	125.76 nM	48
$\{[Zn_2(5\text{-}AIA)_2(DPTTZ)]\cdot DMF\}_n$	Hg^{2+}	4.2×10^4	2.174 nM	49
$\{[Zn(4bpyttz)(FDBA)_2]\cdot 2H_2O\}_n$	Fe^{3+}	8.8527×10^3	125.2 μM	50
	CrO_4^{2-}	9.7079×10^3	114.2 μM	
	$Cr_2O_7^{2-}$	1.3268×10^4	83.5 μM	
$[Cd(4bpyttz)(OBA)]_n$	4-NA	1.03×10^5	0.52 μM	51
	CrO_4^{2-}	2.93×10^4	1.37 μM	
$\{[Zn_2(NDC)_2(4bppyttz)]\cdot 1.5DMF\}_n$	Al^{3+}	4.66×10^3	2.9 μM	52
	CrO_4^{2-}	8.32×10^3	3.4 μM	
	MnO_4^-	1.51×10^4	3.0 μM	
	$Cr_2O_7^{2-}$	7.36×10^3	2.2 μM	
$\{[Zn_2(4bpyttz)_2(BDC)_2]\cdot 2(DMF)\cdot 0.5(H_2O)\}_n$	TNP	3.257×10^4	0.93 μM	53
	NZF	1.726×10^4	0.91 μM	
$\{[Cd_2(4bpyttz)_2(BDC)_2]\cdot 2(DMF)\}_n$	TNP	4.063×10^4	0.90 μM	
	NZF	4.538×10^4	0.85 μM	
$\{[Zn_2(OBA)_2(4bpyttz)]\cdot 2DMF\}_n$	Co^{2+}	3.13×10^3	1.14 μM	54
	NZF	3.02×10^3	0.14 μM	
	NFT	1.22×10^4	0.072 μM	
H_2TTZ@PCN-700	DCF	—	0.9 μM	55

through adsorption by organisms further amplifies their impact, potentially leading to severe health consequences in humans. Therefore, the accurate and selective detection of heavy metal ions is crucial. Luminescent MOFs have emerged as highly effective platforms for detecting these pollutants.

Mercury (Hg^{2+}) detection

Among heavy metal ions, mercury (Hg^{2+}) is particularly hazardous, with contamination arising from natural and anthropogenic sources. The conversion of inorganic Hg^{2+} to methylmercury ($MeHg^+$) by bacteria enhances its bioavailability and promotes its accumulation in food chains, leading to toxic effects at higher trophic levels. Luminescent MOF-based sensors are promising for Hg^{2+} detection due to their high sensitivity and selectivity. The TTZ moiety, which features nitrogen and sulfur heteroatoms, is particularly effective due to its strong affinity for Hg^{2+}, making it an ideal ligand in luminescent MOFs design.

Saha and co-workers introduced a luminescent MOF, $[Zn_2(NDC)_2(4bpyttz)]_n$,[46] where naphthalene dicarboxylate (NDC) acts as the antenna chromophore, and the thiazolothiazole ligand 4bpyttz serves as the energy acceptor and emitter. This MOF exhibits efficient energy transfer between the donor and acceptor due to spectral overlap, enabling selective Hg^{2+} detection with a limit as low as 10^{-6} M (Fig. 4). The presence of Hg^{2+} induces a red shift and fluorescence quenching, while other metal ions only cause minor quenching without spectral shifts.

Furthermore, the stable vacant binding sites (nitrogen and sulfur atoms) of the thiazolothiazole ligand (4bpyttz) in LMOFs play a crucial role in its excellent sensing performance for Hg^{2+}. Similarly, Yu, Feng and co-workers reported $[Zn(4bpyttz)(5\text{-}OH\text{-}IPA)]_n$,[48] a MOF with exceptional selectivity and sensitivity for Hg^{2+}, with a Stern–Volmer constant (K_{sv}) of 8.43×10^4 M^{-1} and a detection limit of 125.76 nM. This sensor demonstrated reliable recovery in real water samples, highlighting its potential for environmental monitoring. Additionally, Wang and co-workers[47] presented $\{\{Ag_4(4bpyttz)_4[Ag(PMo_{12}O_{40})_2]\}\cdot Ag(4bpyttz)\cdot 2(4bpyttz)\cdot 6H_2O\}_n$, a MOF featuring a Keggin-dimer structure. This framework exhibited a 72.2% decrease in fluorescence intensity upon exposure to Hg^{2+} ions, showcasing its selective sensing capabilities. Meanwhile, Mandal and co-workers[49] described a Zn-based MOF, $\{[Zn_2(5\text{-}AIA)_2(4bpyttz)]\cdot DMF\}_n$, composed of 5-aminoisophthalic acid (5-AIA) and 4bpyttz ligands. This MOF detected Hg^{2+} through fluorescence quenching, achieving an impressive detection limit of 2.174×10^{-9} M. The sensing mechanism was attributed to the interaction

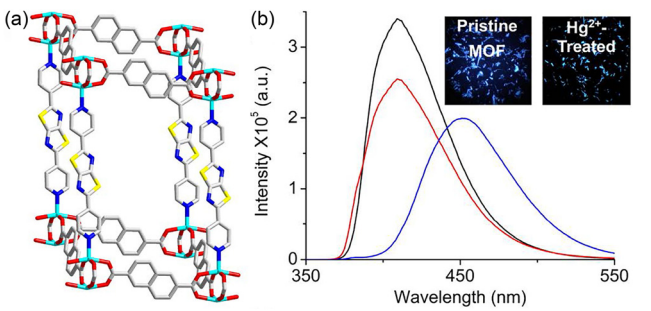

Fig. 4 (a) Single crystal structures of $Zn_2(NDC)_2(4bpyttz)$. (b) Fluorescence intensity of $Zn_2(NDC)_2(4bpyttz)$ suspension (0.1 mg mL^{-1} in DMF) with increasing concentration of $Hg(OTf)_2$. Inset: fluorescence microscopy images of pristine (left) and Hg^{2+} treated $Zn_2(NDC)_2(4bpyttz)$. Reproduced with permission from ref. 46. Copyright 2019, American Chemical Society.

between Hg^{2+} and oxygen coordination centers on the 5-AIA ligands rather than the TTZ sulfur and nitrogen centers.

Detection of other metal ions

The detection of other toxic metal ions, like Fe^{3+}, Co^{2+}, and different oxoanion species such as Cr(VI) and Mn(VII), holds equal significance.

Das and co-workers[50] reported a 3D MOF $\{[Zn(4bpyttz)(FDBA)_2]\cdot 2H_2O\}_n$, capable of detecting Fe^{3+} and $Cr_2O_7^{2-}/CrO_4^{2-}$ with detection limits of 125.2 μM and 114.2/83.5 μM, respectively (Fig. 5). The fluorescence quenching mechanism was attributed to competitive excitation energy absorption and Förster resonance energy transfer. Tadjarodi and co-workers[51] designed a 2D framework $[Cd(4bpyttz)(OBA)]_n$, which demonstrated high sensitivity for detecting 4-nitroaniline (4-NA) and CrO_4^{2-}. The MOF achieved K_{sv} values of 1.03×10^5 M^{-1} for 4-NA and 2.93×10^4 M^{-1} for CrO_4^{2-}, with detection limits of 0.52 μM and 1.37 μM, respectively. Gao and co-workers[43] reported a stable 2D MOF, $\{[Zn(TTVTC)]\cdot 4H_2O\}_n$, based on a TTZ-extended viologen tetracarboxylic acid ligand. This MOF exhibited superior sensitivity and recyclability for CrO_4^{2-} and $Cr_2O_7^{2-}$ detection with detection limits of 0.31 μM and 0.41 μM, respectively. The sensing mechanism was attributed to competitive optical absorption.

Huang and co-workers developed a Zn-MOF $\{[Zn_2(NDC)_2(4bppyttz)]\cdot 1.5DMF\}_n$ with a three-fold interpenetrated pillared-layer structure (Fig. 6).[52] This MOF demonstrated turn-on fluorescence for Al^{3+} and turn-off fluorescence for oxoanion species like CrO_4^{2-}, $Cr_2O_7^{2-}$, and MnO_4^-. Detection limits for Al^{3+}, CrO_4^{2-}, MnO_4^-, and $Cr_2O_7^{2-}$ were 2.9, 3.4, 3.0, and 2.2 μM, respectively. The sensing mechanism involved bonding interactions, electron transfer, and absorbance-related fluorescence enhancement.

These studies underscore the versatility and effectiveness of TTZ-based MOFs for the selective detection of various metal ions, highlighting their potential for environmental and analytical applications.

Sensing organic pollutants

The detection of organic pollutants, particularly nitroaromatic compounds and nitrofuran antibiotics, is of significant environmental and biomedical importance. Metal–organic frameworks (MOFs) have demonstrated exceptional capabilities in this regard due to their tunable structures and luminescent properties.

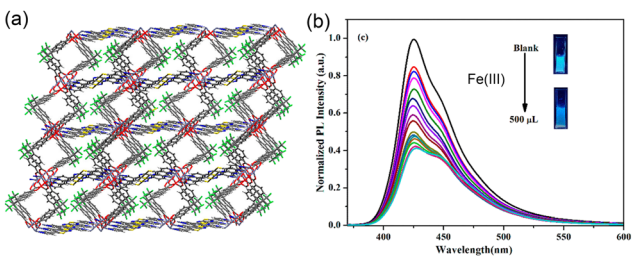

Fig. 5 (a) $\{[Zn(4bpyttz)(FDBA)_2]\cdot 2H_2O\}_n$ along the *b* axis. (b) Luminescence responses of $\{[Zn(4bpyttz)(FDBA)_2]\cdot 2H_2O\}_n$ with the gradual additions of aqueous Fe(III). Reproduced with permission from ref. 50. Copyright 2019, American Chemical Society.

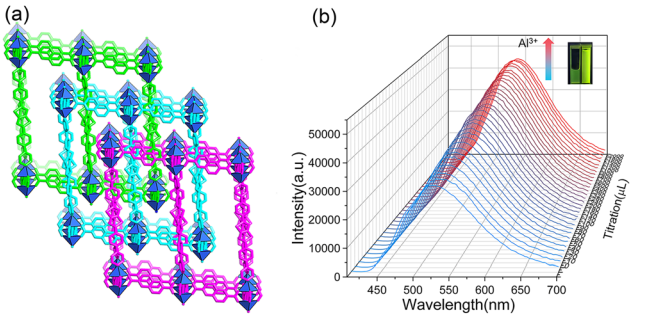

Fig. 6 (a) The threefold interpenetration of the thiazolothiazole based Zn-MOF. (b) Fluorescence spectra intensity of the Zn-MOF in aqueous solution with adding concentrations of Al^{3+} showing turn-on effects. Reproduced with permission from ref. 52. Copyright 2023, Elsevier B.V.

Zang, Du and co-workers[53] developed two three-dimensional MOFs, $\{[Zn_2(4bpyttz)_2(BDC)_2]\cdot 2(DMF)\cdot 0.5(H_2O)\}_n$ and $\{[Cd_2(4bpyttz)_2(BDC)_2]\cdot 2(DMF)\}_n$, featuring the *pcu* topology and strong fluorescence properties. These MOFs exhibit efficient luminescence quenching in the presence of trace amounts of nitroaromatics such as 2,4,6-trinitrophenol (TNP). For the Zn-MOF, the Stern–Volmer quenching constant (K_{sv}) for TNP was determined to be 3.257×10^4 M^{-1}, with a detection limit (LOD) of 0.93 μM. The Cd-MOF demonstrated slightly enhanced performance, with a K_{sv} of 4.063×10^4 M^{-1} and a LOD of 0.90 μM. These MOFs were also effective in detecting nitrofuran antibiotics, including nitrofurazone (NZF). For the Zn-MOF, the LOD and K_{sv} for NZF were 0.91 μM and 1.726×10^4 M^{-1}, respectively, while the Cd-MOF exhibited higher sensitivity with a LOD of 0.85 μM and a K_{sv} of 4.538×10^4 M^{-1}. The luminescence quenching mechanisms involve dynamic and static quenching, primarily driven by photoinduced electron transfer (PET) and Förster resonance energy transfer (FRET) processes. Tadjarodi further explored a two-dimensional MOF, $[Cd(4bpyttz)(OBA)]_n$, demonstrating remarkable sensitivity to 4-nitroaniline (4-NA) with a K_{sv} of 1.03×10^5 M^{-1}.

Huang and co-workers recently reported a three-dimensional MOF, $\{[Zn_2(OBA)_2(4bpyttz)]\cdot 2DMF\}_n$, with a unique 6-c net structure and a novel topology denoted as $\{4^4\cdot 6^{10}\cdot 8\}$.[54] The MOF exhibited high selectivity and multi-responsiveness, making it effective for detecting Co^{2+} ions and nitrofuran antibiotics, such as NZF and nitrofurantoin (NFT), in aqueous media. The detection limits for Co^{2+}, NZF, and NFT were determined to be 1.14, 0.14, and 0.072 μM, respectively. Importantly, the MOF-derived fluorescence test papers and composite films were developed for visual detection of Co^{2+}, NZF, and NFT (Fig. 7). These practical sensing platforms significantly enhance the applicability of MOFs in real-world environmental monitoring and medical diagnostics.

The development of MOF-based ion detection test papers or thin films represents an important step toward real-world

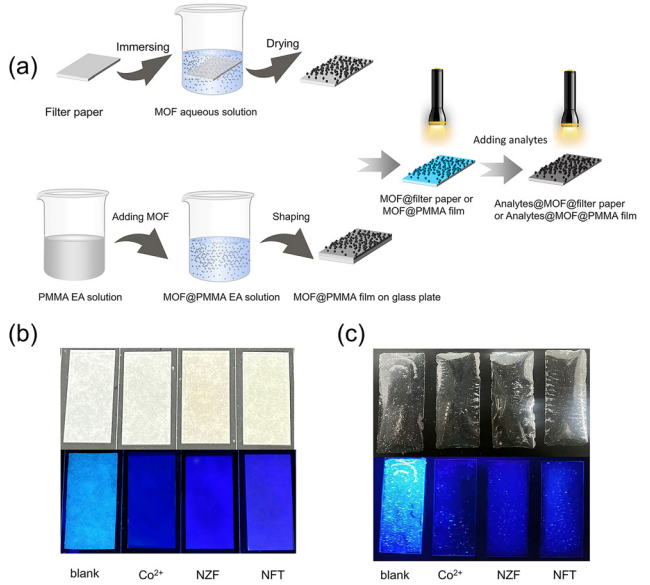

Fig. 7 (a) The procedure for making MOF-based fluorescence test papers and composite films. (b) and (c) Pictures of the MOF-based fluorescence test papers and composite films for the detection of the Co^{2+} ion and antibiotics. Reproduced with permission from ref. 54. Copyright 2024, Elsevier B.V.

applications, as these materials allow for rapid, on-site, and cost-effective sensing of pollutants. The combination of high sensitivity, selectivity, and the ability to fabricate portable sensing devices underscores the potential of MOF-based systems in environmental and biomedical fields.

Galli, Piccirillo, Rossin and co-workers[55] presents the thiazolo[5,4-*d*]thiazole-2,5-dicarboxylic acid (H_2TTZ)-functionalized Zr(IV) mixed-linker MOF (H_2TTZ@PCN-700), synthesized *via* solvent-assisted ligand incorporation (SALI). H_2TTZ@PCN-700 exhibits a high diclofenac sodium (DCF) adsorption capacity (263.2 mg g^{-1}) in water, driven by strong host–guest interactions and a hierarchical micro/mesoporous structure (BET area: 757 m^2 g^{-1}). While H_2TTZ@PCN-700 shows ligand-centered luminescence, its emission quenching mechanism for DCF sensing (LOD: 9.0×10^{-5} M) stems from HOCO localization on non-luminescent Me_2-$BPDC^{2-}$ linkers. Selective DCF detection over other pollutants and partial desorption reversibility (<10%) highlight its dual wastewater remediation potential. Its thermal stability (T_{666}: ~770 K) and water resistance position H_2TTZ@PCN-700 as a robust adsorbent, with future efforts targeting recyclability and enhanced sensing synergy.

Photochromism

Photochromic behavior is a hallmark property of TTZ-based materials. This phenomenon is often driven by photoinduced electron transfer (PET) processes that alter their electronic states, leading to visible color changes.

In 2019, Gao and co-workers[56] synthesized a tetracarboxylate ligand, $[H_4TTVTC]Cl_2$, derived from thiazolothiazole-extended viologen (Fig. 8). They further prepared a three-dimensional metal–organic framework (MOF), $\{[Cd_2(TTVTC)Cl_2(H_2O)_3]\cdot 2H_2O\}_n$, which features a (10,3)-*d* framework with sixfold interpenetration. This MOF demonstrated reversible photochromism, changing from yellow-orange to green upon photoinduced electron transfer from carboxylate groups to TTV^{2+} centers.

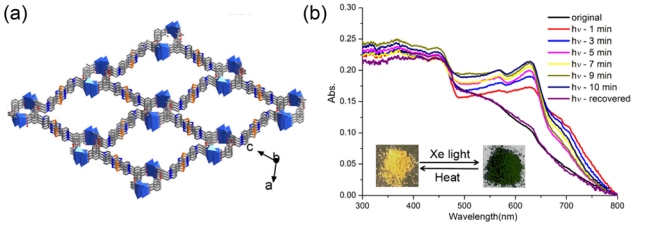

Fig. 8 (a) A single 3D framework along the *b* axis. (b) UV-vis spectra and photographs of the color changed before and after Xe light irradiation. Reproduced with permission from ref. 56. Copyright 2019, American Chemical Society.

Wang and co-workers[57] reported a bicarboxylate ligand based on thiazolothiazole-extended viologen and its derived 3D MOF, $\{[Zn(4,4'\text{-bpy})(TTVP)]\cdot(NO_3)_2\cdot 4H_2O\}_n$, which has an eightfold interpenetrated structure. Another structure, $\{[Zn(Hbtc)(TTVP)_{0.5}]\}_n$, was synthesized as a two-dimensional layered MOF. Both compounds exhibited photochromism, but the latter compound showed a faster photochromic response due to the shorter distance between electron donors (*O*-carboxylate) and acceptors (*N*-pyridinium) within TTVP molecules.

Liu and co-workers[58–60] successfully obtained a series of photochromic compounds by incorporating auxiliary carboxylic acid ligands with thiazolothiazole-extended viologen (TTVP). Interestingly, Wang and co-workers[61] reported two MOFs, $\{[Cd(TTVP)_{0.5}(2,6\text{-NDC})(H_2O)]\cdot 0.5DMF\}_n$ and $\{[Cd(TTVP)_{0.5}(4,4'\text{-BPC})(H_2O)_2]\cdot 0.5H_2O\}_n$, which exhibited both photochromic behavior and photo-controlled fluorescence. This synergistic response was attributed to the formation of colored anionic $[TTVP]^{\bullet-}$ radicals *via* PET processes.

Ren, Wang and co-workers[62] synthesized *N*,*N*′-2,5-bis(3-pyridinium)thiazolo[5,4-*d*]thiazole dipropionate based on the 3bpyttz ligand, $(mTTVPA)(HSO_3)_2$, and two MOFs, $\{[Cd(mTTVPA)Br_2]\cdot H_2O\}_n$ and $\{[Zn(mTTVPA)Br_2]\cdot H_2O\}_n$. These compounds displayed photochromic properties driven by PET, generating radical species responsible for observable color changes.

Electrochromism

Electrochromic properties of thiazolothiazole-based materials stem from their redox-active ligands and robust frameworks that facilitate charge migration.

D'Alessandro, Kepert and co-workers reported Zn/Cd-MOFs based on TTZ derivative ligands (4bppyttz and 4bmppyttz).[63,64] These studies investigated intervalence charge transfer (IVCT) phenomena within the redox-active frameworks. Their coplanar

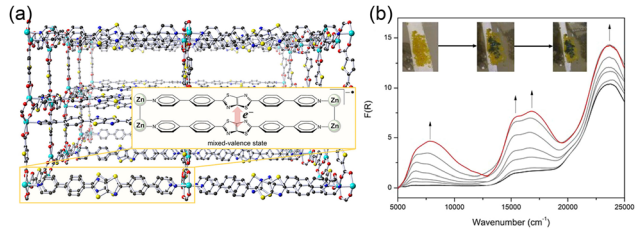

Fig. 9 (a) Crystal structure of the framework displaying the cofacial alignment of the 4bppyttz ligands along the *c* axis. (b) Room temperature solid-state spectroelectrochemistry with photographs capturing the framework transitioning from yellow (neutral) to dark green (mixed-valence state). Reproduced with permission from ref. 64. Copyright 2018, American Chemical Society.

structures enabled efficient charge migration, as confirmed through computational models that quantified the extent of charge transfer and unveiled novel mechanisms of charge migration in MOFs. Similarly, the redox-active MOFs $[Zn_2(4bppyttz)_2(SDC)_2]_n$ and $[Cd_2(4bppyttz)_2(SDC)_2]_n$ demonstrated distinct electrochromic behavior.[65] The electrochromic response was attributed to reversible redox processes and electron mobility facilitated by the TTZ ligands.

Therefore, TTZ-extended viologen-based materials represent a promising class of multi-stimuli responsive materials. Their photochromic and electrochromic behaviors, driven by mechanisms such as PET and IVCT, open new avenues for applications in sensors, displays, and energy storage devices. Further exploration of ligand design and framework engineering could lead to improved responsiveness and broadened functionality (Fig. 9).

Fluorescence bioimaging

MOFs incorporating thiazolo[5,4-*d*]thiazole derivatives have emerged as promising candidates for bioimaging applications, owing to their exceptional optical properties.

A novel UiO-type MOF (ZrMOF) based on the thiazolo[5,4-*d*]thiazole bicarboxylate ligand responsive to higher-order multiphoton excited fluorescence (H-MPEF) was successfully synthesized (Fig. 10), but single crystal structure data could not be obtained.[41] The framework design leveraged the extended π-electron systems of the thiazolo[5,4-*d*]thiazole ligands, which facilitated enhanced charge transfer and increased dipole moments while reducing π–π stacking interactions. These structural attributes endowed the MOF with outstanding fluorescence in the near-infrared II (NIR-II) region, making it a valuable tool for light-induced fluorescence imaging in bioimaging applications.

Photon upconversion

Photon upconversion (UC), a process in which low-energy photons are converted into high-energy photons, has significant implications for various scientific and technological fields, including photochemistry, solar energy harvesting, and bioimaging.

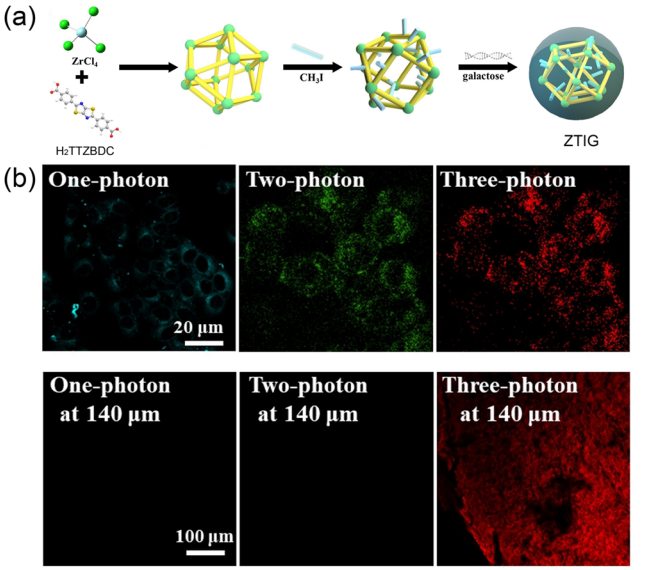

Fig. 10 (a) Synthesis route of galactose-modified zirconium MOF (**ZTIG**). (b) One-/two-/three-photon CLSM images of Hep G2 cell treatment with ZrMOF upon the irradiation of 405 nm, 860 nm, and 1250 nm. Reproduced with permission from ref. 41. Copyright 2022, John Wiley & Sons, Inc or related companies.

Stoddart and co-workers[66] reported a Zn-based MOF (ZnMOF) designed for TTA-UC, constructed from tetra(4-carboxyphenyl)porphyrin (H_4TCPP) sensitizers and dipyridylthiazole (4bpyttz) quenchers (Fig. 11). In this MOF, zinc ions coordinate the sensitizers and quenchers into a propeller-like arrangement within a two-dimensional layered structure. The thiazole pillars connect these layers, and the high ratio of quenchers to sensitizers (5,1) promotes an organized sensitizer arrangement, optimizing Dexter energy transfer. This structural precision achieves an impressive TTA-UC efficiency of 1.95% at an excitation power density of 25 mW cm^{-2}. When exciting the low-energy Q bands of Zn-TCPP (565 and 602 nm), blue emission based on 4bpyttz upconversion (465 nm) is observed. The presence of this emission is direct evidence that the MOF exhibits photon upconversion properties.

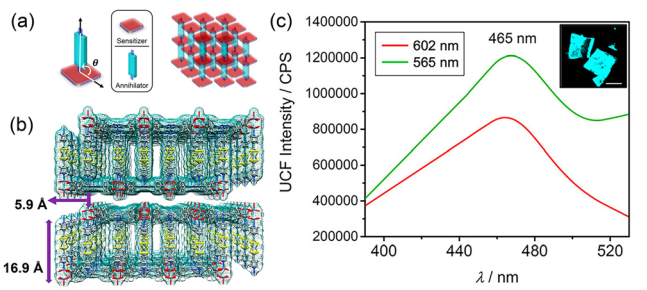

Fig. 11 (a) Axial coordination of annihilators to porphyrin sensitizers as a well-established strategy for constructing TTA-UC systems in solution. (b) The distance between the 2D sheets and the interlayer distance. (c) Fluorescence spectra of the MOF suspension in $(Me)_2CO$. Inset: confocal image of the MOF crystals excited by a 561 nm laser. Reproduced with permission from ref. 66. Copyright 2019, American Chemical Society.

Magnetic properties

The integration of thiazolo[5,4-*d*]thiazole into MOFs also yields intriguing magnetic properties, particularly through spin-crossover behavior and the unique characteristics of lanthanide ions.

Tao and co-workers[67] synthesized a two-dimensional grid-like coordination polymer, $\{[Fe(NCBH_3)_2(4bpyttz)_2]\cdot 4CHCl_3\}_n$, which displayed a one-step complete spin crossover. Remarkably, this transition exhibited a large hysteresis loop (64 K) and a temperature-induced excited spin-state trapping effect below 91 K, underscoring its potential in molecular magnetism applications. Structural analysis reveals that the large hysteresis arises from significant ligand rotation and grid deformation, which enhance cooperative interactions. This work highlights the potential of rigid bis-monodentate ligands in stabilizing wide hysteresis loops, advancing the development of SCO-based functional materials (Fig. 12).

Incorporating thiazolo[5,4-*d*]thiazole ligands (H_2TTZ or 4bpyttz) further highlighted the magnetic characteristics of lanthanide MOFs.[68,69] These MOFs inherit the characteristic magnetic properties of lanthanide ions.

Adsorption separation

Adsorptive separation presents a promising alternative to mitigate the high energy consumption and capital costs of the distillation separation of similar physicochemical properties of these molecules. However, achieving efficient and selective adsorption remains a significant challenge due to the similar physicochemical properties of these molecules, necessitating the development of highly selective adsorbents with tailored pore structures and surface functionalities. Zhang, Chen and co-workers[70] reported a flexible metal–organic framework (MOF) material $[Zn_2(Cl\text{-}BDC)_2(4bpyttz)]_n$ with a doubly interpenetrated pillared paddle wheel structure for realizing efficient C_3H_6/C_3H_8 separation. By carefully selecting appropriate linkers, the framework is designed with

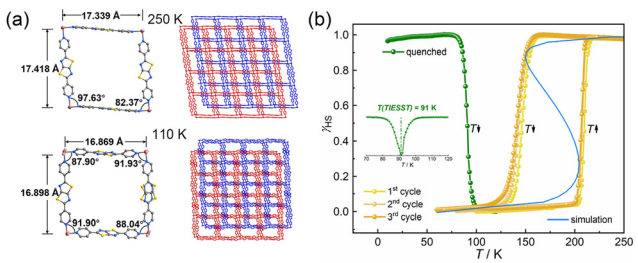

Fig. 12 (a) The Fe···Fe distances and Fe···Fe···Fe angles within the network, as well as the stacking structures of the quadrilateral networks for $[Fe(NCBH_3)_2(4bpyttz)_2]\cdot 4CHCl_3$ at 250 K and 110 K. (b) The temperature-induced SCO behavior depicted through three cycles, with simulation of SCO cooperativity in light blue and the temperature-induced excited spin-state trapping (TIESST) effect in green. The inset displays a $d(\gamma_{HS})/dT$ *versus* T plot for the thermally quenched sample. Reproduced with permission from ref. 67. Copyright 2022, American Chemical Society.

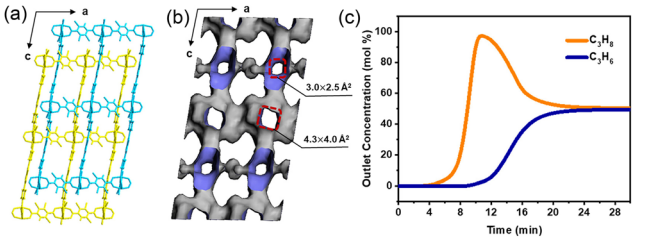

Fig. 13 (a) Interpenetrated framework of the MOF viewed along the *b*-axis. (b) Channels and pore apertures of the MOF along the *b*-axis. (c) Column breakthrough curve of the MOF with equal molar amounts of C_3H_6 and C_3H_8. Reproduced with permission from ref. 70. Copyright 2020, American Chemical Society.

small pore apertures that significantly enhance propylene adsorption over propane. This selective adsorption is primarily governed by the molecular sieving effect of the flexible framework, which enables precise discrimination between the two gases. Furthermore, column breakthrough experiments have demonstrated that this separation remains highly efficient under dynamic conditions, highlighting the practical applicability of the material in real-world separation processes (Fig. 13).

Catalyst

In 2018, Lin and co-workers[71] reported a dual-continuous donor–acceptor (D–A) hybrid structure, $\{[Cu_2(4bpyttz)(CN)_2]_{0.5}(4bpyttz)\}_n$, based on the 2,5-bis(4-pyridyl)thiazolo[5,4-*d*]thiazole ligand, where 4bpyttz and Cu^{2+} act as the electron donor and acceptor, respectively. This hybrid structure demonstrated photocatalytic activity for the degradation of methylene blue (MB), rhodamine B (RhB), and methyl orange (MO). The strong coordination interactions and cation–π interactions between the two semiconductor components contributed to its enhanced photocatalytic performance compared to the individual semiconductors 4bpyttz and CuCN.

Zang, Li and co-workers[72] reported the MOFs $\{[Zn(4bpyttz)(2\text{-}NH_2\text{-}BDC)]\cdot(DMF)\}_n$ and $\{[Cd(4bpyttz)(2\text{-}NH_2\text{-}BDC)]\cdot(DMF)\cdot 0.5(H_2O)\}_n$ with 2-fold interpenetrated three-dimensional bi-pillared-layer framework, which was constructed using the nitrogenous linkers 4bpyttz and 2-amino-1,4-benzenedicarboxylic acid ($2\text{-}NH_2\text{-}H_2BDC$). Given their good chemical stabilities, high thermal stabilities, and exposed nitrogen sites, the MOFs will provide a multifunctional platform for adsorbing CO_2 selectively and catalysing the Knoevenagel reaction effectively.

Neogi, Kundu and co-workers[73] demonstrate a novel linker scissoring strategy to develop a robust MOF [Co(2-ATA)(4bpyttz)] from the assembly of Co(II) ions with an electroactive 4bpyttz (NS atoms) linker and a H-bond operative 2-ATA (2-aminoterepthalic acid) ligand. The activated framework exemplifies highly efficient oxygen evolution reactions (OERs) with a low overpotential of 391 mV and an appreciable Tafel slope of 85 mV dec^{-1}. And then Neogi, Kundu and co-workers[74] reported a 2D layer-stacked Co(II)–organic framework (FCG-2) by C_3 symmetric tricarboxylic acid (H_3TCA) and 4bpyttz

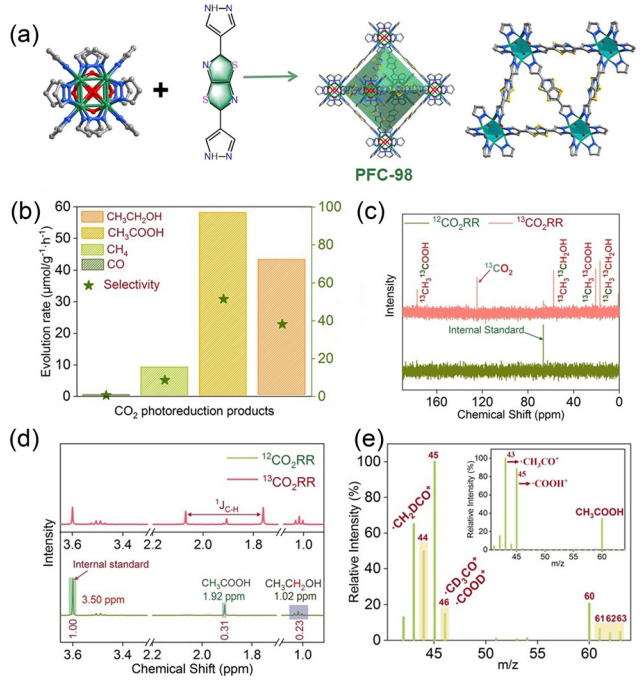

Fig. 14 (a) Synthesis routes and crystal structure of PFC-98. Gas–solid photocatalytic CO_2RR performance of PFC-98. (b) Evolution rate and selectivity of reduction products over 10 hours. (c) ^{13}C NMR spectra of liquid products from photoreduction with $^{12}CO_2$ and $^{13}CO_2$. (d) ^1H NMR of liquid products with $^{12}CO_2$ and $^{13}CO_2$ in the presence of H_2O. (e) GC-MS spectrum of liquid product with D_2O and CO_2 (inset: GC-MS result of CH_3COOH).

functionalized strut manifest bimodal redox-activity as a water oxidation catalyst in alkaline medium with 375 mV overpotential, 78 mV per dec Tafel slope, 81.25% faradaic efficiency (FE) and 23 h of chronopotentiometric stability. The Ni^{2+} grafted FCG-2(M^{2+}@FCG-2) exhibits bifunctional acid–base properties, enabling size-selective deacetalization–Knoevenagel reaction with high yield and multicyclic usability under mild conditions.

Zhang and co-workers[44] reported that a MOF Cd-TTZBDP based on the TTZ viologen carboxylic acid ligand can be used to simulate the electron transfer chain (ETC) in biological systems. The stacking mode of TTZ dyes in the material promotes light-induced charge separation across ligands, as well as subsequent delocalization of electrons and protons along the stacked D/A columns, inhibiting recombination of separated charge carriers. This enables spatial isolation of the reduction and oxidation centers, visualizing the photocatalytic steps through long-lasting photochromism of the MOF.

Wu, Liu and co-workers[75] have described a NiTTZ MOF (PFC-98) as a model photocatalyst, with the material possessing energy levels that align with the lowest unoccupied node and linker orbitals. This alignment creates a delocalized lowest unoccupied crystal orbital (LUCO) over both the node and linker, facilitating charge separation and enabling abundant electrons to gather at the catalytic sites for multi-electron transfer processes. PFC-98 exhibits outstanding overall CO_2 photocatalytic performance, and demonstrated remarkable selectivity (89.68%) and productivity (58.14 μmol g^{-1} h^{-1}) for C_2 products, specifically ethanol and acetic acid, in the absence of sacrificial agents (Fig. 14).

Conclusions and outlook

In recent years, metal–organic framework (MOF) materials based on thiazolo[5,4-*d*]thiazole (TTZ) derivatives have been widely used in various fields due to their excellent structural tunability and outstanding photoelectrochemical properties. These TTZ-based MOFs show great potential in solving technical challenges in areas such as fluorescence sensing, photochromism, adsorption separation, photon upconversion, catalysis, and fluorescence bioimaging.

Despite the notable achievements in TTZ derivative-based MOFs, there are still challenges and room for development:

(1) Designing and optimizing material properties: the rational design of TTZ-based ligands provides a pathway for constructing structurally diverse and functionally advanced MOFs. Initially, by diversifying the types of TTZ based bipyridine or dicarboxylic acid ligands through molecular assembly and design, including the incorporation of large conjugated groups, electron-donating, electron-withdrawing, and other functional groups to further control the framework's pore structure, electronic or charge distribution, and properties, such as absorption and emission, in order to extend and enhance their performance. Designing ligands that allow for precise control of MOF architectures, including pore size, connectivity, and dimensionality, enabling tailored applications in gas storage, separation, or catalysis. Increasing the π-conjugation of TTZ ligands to improve their electronic communication, luminescence properties, and interactions with metal nodes. This can not only expand the structural library of TTZ-based MOFs but also provide opportunities for tuning their properties to meet the demands of specific applications.

(2) Deepening functional studies of TTZ-MOFs: the study of MOFs based on TTZ ligands is just beginning. Due to the superior performance of TTZ ligands, research on this type of material is expected to grow. Currently, the focus is mainly on structural characterization, fluorescence sensing, photochromism, and catalysis, with fewer studies in other areas.

(3) Incorporating artificial intelligence (AI) and machine learning (ML): the integration of MOFs, not limited to TTZ based MOFs, with AI and ML is an exciting frontier in materials science. Researchers can use AI and ML algorithms to predict MOF properties based on their molecular structure, such as pore size, surface area, and stability. Machine learning models, including deep learning, can be trained on large datasets to accelerate the discovery of new MOFs with specific functionalities. By combining data-driven approaches with traditional chemical knowledge, the development of MOFs for specific applications can be streamlined, reducing experimental costs and time. Incorporating AI and ML into MOF research will lead to more efficient, scalable, and targeted material design, potentially revolutionizing industries like energy, environmental sustainability, and medicine.

Overall, MOF materials derived from TTZ show great promise for various applications. As material design and performance continue to improve, they are expected to have a significant impact in areas such as materials, energy, environment, and biomedicine.

Abbreviation

4bpyttz	2,5-Di(pyridin-4-yl)thiazolo[5,4-*d*]thiazole
3bpyttz	2,5-Di(pyridin-3-yl)thiazolo[5,4-*d*]thiazole
bpzttz	2,5-Di(1*H*-pyrazol-4-yl)thiazolo[5,4-*d*]thiazole
4bppyttz	2,5-Bis(4-(pyridin-4-yl)phenyl)thiazolo[5,4-*d*]thiazole
4bfppyttz	2,5-Bis(3-fluoro-4-(pyridin-4-yl)phenyl)thiazolo[5,4-*d*]thiazole
4bmppyttz	2,5-Bis(3,5-dimethyl-4-(pyridin-4-yl)phenyl)thiazolo[5,4-*d*]thiazole
3bppyttz	2,5-Bis(3-(pyridin-4-yl)phenyl)thiazolo[5,4-*d*]thiazole
tppttz	*N*,*N*′-(Thiazolo[5,4-*d*]thiazole-2,5-diylbis(4,1-phenylene))bis(*N*-(pyridin-4-yl)pyridin-4-amine)
H_2TTZ	Thiazolo[5,4-*d*]thiazole-2,5-dicarboxylic acid
H_2TTZBDC	4,4′-(Thiazolo[5,4-*d*]thiazole-2,5-diyl)dibenzoic acid
TTVP	4,4′-(Thiazolo[5,4-*d*]thiazole-2,5-diyl)bis(1-(2-carboxyethyl)pyridin-1-ium) chloride
mTTVPA	3,3′-(Thiazolo[5,4-*d*]thiazole-2,5-diyl)bis(1-(carboxymethyl)pyridin-1-ium)
TTVTC	4,4′-(Thiazolo[5,4-*d*]thiazole-2,5-diyl)bis(1-(3,5-dicarboxybenzyl)pyridin-1-ium) chloride
TTZBDP	4,4′-(Thiazolo[5,4-*d*]thiazole-2,5-diyl)bis(1-(3,5-dicarboxyphenyl)pyridin-1-ium) chloride
H_2BDC	Erephthalic acid
2-MBDC	2-Methylterephthalic acid
BMBDC	2,5-Dimethylterephthalic acid
BOBDC	2,5-Dihydroxyterephthalic acid
ABDC	2-Aminoterephthalic acid
ClBDC	2-Chloroterephthalic acid
1,4-H_2NDC	Naphthalene-1,4-dicarboxylic acid
H_2NDC	Naphthalene-2,6-dicarboxylic acid
1,3-BDC	Isophthalic acid
5-MBDC	5-Methylisophthalic acid
5-AIA	5-Aminoisophthalic acid
5-OH-IPA	5-Hydroxyisophthalic acid
H_2FDC	Furan-2,5-dicarboxylic acid
H_2TDC	Thiophene-2,5-dicarboxylic acid
H_2SD	Selenophene-2,5-dicarboxylic acid
H_2OBA	4,4′-Oxydibenzoic acid
H_2FDBA	4,4′-(Perfluoropropane-2,2-diyl)dibenzoic acid
H_2BPDC	[1,1′-Biphenyl]-4,4′-dicarboxylic acid
H_2CBBA	4,4′-((((1*R*,2*R*)-Cyclohexane-1,2-diyl)bis(azanediyl))bis(carbonyl))dibenzoic acid
H_3TCA	4,4′,4″-Nitrilotribenzoic acid
H_4TCPPA	4,4′,4″,4‴-(Pyrazine-2,3,5,6-tetrayl)tetrabenzoic acid
H_4TCPP	4,4′,4″,4‴-(Porphyrin-5,10,15,20-tetrayl)tetrabenzoic acid

Data availability

Data will be made available on request.

Author contributions

Both authors contributed to the manuscript. And both authors read, revised, and approved the final version for publication.

Conflicts of interest

There are no conflicts to declare.

Acknowledgements

We acknowledge the National Natural Science Foundation of China (grant no. 21601153) and the Qing-Lan Project of Jiangsu Province (X.-C. Huang).

Notes and references

1 H.-C. Zhou, J. R. Long and O. M. Yaghi, *Chem. Rev.*, 2012, **112**, 673–674.
2 H. Furukawa, K. E. Cordova, M. O'Keeffe and O. M. Yaghi, *Science*, 2013, **341**, 1230444.
3 C. Jiang, X. Wang, Y. Ouyang, K. Lu, W. Jiang, H. Xu, X. Wei, Z. Wang, F. Dai and D. Sun, *Nanoscale Adv.*, 2022, **4**, 2077–2089.
4 L. E. Kreno, K. Leong, O. K. Farha, M. Allendorf, R. P. Van Duyne and J. T. Hupp, *Chem. Rev.*, 2011, **112**, 1105–1125.
5 Y. Zhang, S. Yuan, G. Day, X. Wang, X. Yang and H.-C. Zhou, *Coord. Chem. Rev.*, 2018, **354**, 28–45.
6 A. Bavykina, N. Kolobov, I. S. Khan, J. A. Bau, A. Ramirez and J. Gascon, *Chem. Rev.*, 2020, **120**, 8468–8535.
7 P. P. Mondal, M. Neem, R. Chand, A. Pandit and S. Neogi, *Chem. Mater.*, 2024, **36**, 10451–10473.
8 H. D. Lawson, S. P. Walton, C. Chan and A. C. S. Appl, *Mater. Interfaces*, 2021, **13**, 7004–7020.
9 J. Ephraim, *Ber. Dtsch. Chem. Ges.*, 1891, **24**, 1026–1031.
10 J. R. Johnson and R. Ketcham, *J. Am. Chem. Soc.*, 1960, **82**, 2719–2724.
11 S. Wang, Z. Xie, D. Zhu, S. Fu, Y. Wu, H. Yu, C. Lu, P. Zhou, M. Bonn, H. I. Wang, Q. Liao, H. Xu, X. Chen and C. Gu, *Nat. Commun.*, 2023, **14**, 6891.
12 P. Weng, Y. Guo, K. Wu, X. Wang, G.-Q. Huang, H. Lei, Y. Yuan, W. Lu and D. Li, *J. Mater. Chem. A*, 2023, **11**, 12194–12201.
13 Y.-Y. He, Z.-P. Ma, C.-H. Liu and Y.-Y. Zhu, *ChemCatChem*, 2024, **16**, e202401327.
14 X. Li, Y. Wang, F. Zhang and X. Lang, *Appl. Catal., B*, 2024, **340**, 123190.
15 M. Liu, F. Zhao, Y. Chu, J. Zhao, F. Meng and Y. Han, *Chem. Eng. Sci.*, 2024, **288**, 119827.
16 H. Miao, L. Chen, F. Xing, H. Li, T. Baumgartner and X. He, *Chem. Sci.*, 2024, **15**, 7576–7585.
17 A. K. Sahoo, S. R. Bhatta, A. Karn and J. N. Moorthy, *ACS Appl. Polym. Mater.*, 2024, **6**, 6425–6436.

18 A. K. Sahoo, C. Yadav and J. N. Moorthy, *Appl. Catal., A*, 2024, **671**, 119557.
19 Y. Song, F. Zhao, W. Zhang, J. Zhao, F. Meng and A. Li, *J. Catal.*, 2024, **433**, 115490.
20 L. Yao, S. Liu, L. Li, B. Ge, W. Jiao, S. Zong, X. Song, D. Zhou and Z. Liang, *CCS Chem.*, 2024, **6**, 1721–1730.
21 D. Bevk, L. Marin, L. Lutsen, D. Vanderzande and W. Maes, *RSC Adv.*, 2013, **3**, 11418–11431.
22 C. Yu, Z. Liu, Y. Yang, J. Yao, Z. Cai, H. Luo, G. Zhang and D. Zhang, *J. Mater. Chem. C*, 2014, **2**, 10101–10109.
23 S. Chatterjee, T. Ohto, H. Tada, S. Jinnai and Y. Ie, *ACS Sustainable Chem. Eng.*, 2020, **8**, 19013–19022.
24 U. Olgun, M. Gülfen, H. Burcu Güneser, B. Seçkin Arslan, N. Öztürk, M. Nebioğlu, İ. Şişman, F. Gülsah Akca, E. Uzay Karakaya and H. Gul Yaglioglu, *J. Photochem. Photobiol., A*, 2024, **454**, 115698.
25 W. Peng, J. Xiong, T. Chen, D. Zhao, J. Liu, N. Zhang, Y. Teng, J. Yu and W. Zhu, *RSC Adv.*, 2024, **14**, 8081–8089.
26 Z. Sun, H. Ma, S. Yang, Y. Cho, S. Lee, J. Park, T. L. H. Mai, W. Kim, S. Jeong, S. Kim and C. Yang, *Adv. Funct. Mater.*, 2024, **34**, 2403093.
27 A. Eckstein-Andicsová, Z. Tokárová, E. Kozma, R. Balogh, A. Vykydalová, W. Mróz and K. Tokár, *New J. Chem.*, 2023, **47**, 11165–11175.
28 A. Jouaiti, D.-C. Huang, V. Giuso, C. Cebrián, P. Mercandelli, K.-H. Wang, C.-H. Chang and M. Mauro, *ACS Appl. Electron. Mater.*, 2023, **5**, 2781–2792.
29 J. Y. Jung, M. Kang, J. Chun, J. Lee, J. Kim, J. Kim, Y. Kim, S.-J. Kim, C. Lee and J. Yoon, *Chem. Commun.*, 2013, **49**, 176–178.
30 Y. Liu, Z. Liang, Z. Li, K. Zhao, Y. Sun, X. Zhang, R. Yang and L. Qu, *Microchem. J.*, 2020, **154**, 104640.
31 V. Kumar, S. Sony, N. Kaur, S. M. Mobin, P. Kaur and K. Singh, *Anal. Chim. Acta*, 2022, **1206**, 339776.
32 O. Turhan, Z. Dikmen and V. Bütün, *J. Photochem. Photobiol., A*, 2023, **443**, 114828.
33 A. F. R. Cerqueira, N. M. M. Moura, M. G. P. M. S. Neves, A. Jorge Parola and A. C. Tomé, *J. Photochem. Photobiol., A*, 2024, **451**, 115490.
34 G. Reginato, A. Mordini, L. Zani, M. Calamante and A. Dessì, *Eur. J. Org. Chem.*, 2016, **2015**, 233–251.
35 Z. Tokárová, A. Eckstein-Andicsová, R. Balogh and K. Tokár, *Tetrahedron*, 2021, **89**, 132155.
36 G. Mercuri, G. Giambastiani and A. Rossin, *Inorganics*, 2019, **7**, 144.
37 J. Preston, *J. Heterocyclic Chem.*, 1965, **2**, 441–446.
38 D. A. Thomas, *J. Heterocyclic Chem.*, 1970, **7**, 457–462.
39 R. C. Knighton, A. J. Hallett, B. M. Kariuki and S. J. A. Pope, *Tetrahedron Lett.*, 2010, **51**, 5419–5422.
40 R. Ziessel, A. Nano, E. Heyer, T. Bura and P. Retailleau, *Chem. – Eur. J.*, 2013, **19**, 2582–2588.
41 B. Li, X. Lu, Y. Tian and D. Li, *Angew. Chem., Int. Ed.*, 2022, **61**, e202206755.
42 F. J. Rizzuto, T. B. Faust, B. Chan, C. Hua, D. M. D'Alessandro and C. J. Kepert, *Chem. – Eur. J.*, 2014, **20**, 17597–17605.
43 P. Li, X.-M. Yin, L.-L. Gao, S.-L. Yang, Q. Sui, T. Gong and E.-Q. Gao, *ACS Appl. Nano Mater.*, 2019, **2**, 4646–4654.
44 L. Ma, T. Zhang, M. Li, X. Zhang, L. Li, Y. Shi, R. Cai, X. Yang and C. Duan, *Chem. Sci.*, 2024, **15**, 17150–17160.
45 A. Aprea, V. Colombo, S. Galli, N. Masciocchi, A. Maspero and G. Palmisano, *Solid State Sci.*, 2010, **12**, 795–802.
46 A. Khatun, D. K. Panda, N. Sayresmith, M. G. Walter and S. Saha, *Inorg. Chem.*, 2019, **58**, 12707–12715.
47 H.-C. Mou, J. Ying, A.-X. Tian, H.-T. Cui and X.-L. Wang, *New J. Chem.*, 2020, **44**, 15122–15130.
48 X. Li, D. Xiu, J. Shi, J. Miao, Y. Yu, H. Song, J. Lin, Q. Feng and H. Yu, *Spectrochim. Acta, Part A*, 2022, **265**, 120367.
49 A. Nath, G. M. Thomas, S. Hans, S. R. Vennapusa and S. Mandal, *Inorg. Chem.*, 2022, **61**, 2227–2233.
50 S. C. Pal, D. Mukherjee and M. C. Das, *Inorg. Chem.*, 2022, **61**, 12396–12405.
51 A. Karbalaee Hosseini and A. Tadjarodi, *Sci. Rep.*, 2023, **13**, 269.
52 X.-C. Huang, Y.-X. Jiang, Z.-J. Han, W. Yong, Q.-X. Huang, W.-X. Shi, X.-R. Chen, J.-J. Kong and H. Wu, *J. Mol. Struct.*, 2023, **1289**, 137424.
53 Z.-W. Zhai, S.-H. Yang, M. Cao, L.-K. Li, C.-X. Du and S.-Q. Zang, *Cryst. Growth Des.*, 2018, **18**, 7173–7182.
54 W. Yong, Q.-C. Huang, H.-Y. Mu, W.-X. Shi, B.-L. Dai, J.-J. Kong, X.-R. Chen and X.-C. Huang, *J. Mol. Struct.*, 2024, **1301**, 137424.
55 G. Provinciali, A. L. Capodilupo, A. Mauri, S. Galli, L. Donà, B. Civalleri, G. Tuci, G. Giambastiani, C. Piccirillo and A. Rossin, *ACS ES T Water*, 2024, **4**, 2339–2351.
56 P. Li, M. Y. Guo, X. M. Yin, L. L. Gao, S. L. Yang, R. Bu, T. Gong and E. Q. Gao, *Inorg. Chem.*, 2019, **58**, 14167–14174.
57 K.-P. Chen, W.-J. Xu, Y. Ma and Q.-L. Wang, *Cryst. Growth Des.*, 2022, **22**, 1024–1031.
58 F. Yang, J. Chen, Y. Fu, J. Wang and J. Liu, *Dyes Pigm.*, 2024, **222**, 111877.
59 F. Yang, J. Chen, J. Wang and J. Liu, *CrystEngComm*, 2023, **25**, 5461–5469.
60 F. Yang, Y. Fu, H. Han, Q. Liu and J. Liu, *Dyes Pigm.*, 2024, **225**, 112076.
61 B. Gao, Y. Sun, G. Li, C. Zhang, X. Liu, Y. Zhou and X. Wang, *Dyes Pigm.*, 2024, **232**, 112490.
62 L. Liu, L.-T. Zhang, F.-C. Yuan, H.-X. Ren, Y. Ma and Q.-L. Wang, *CrystEngComm*, 2024, **26**, 4431–4438.
63 P. W. Doheny, J. K. Clegg, F. Tuna, D. Collison, C. J. Kepert and D. M. D'Alessandro, *Chem. Sci.*, 2020, **11**, 5213–5220.
64 C. Hua, P. W. Doheny, B. Ding, B. Chan, M. Yu, C. J. Kepert and D. M. D'Alessandro, *J. Am. Chem. Soc.*, 2018, **140**, 6622–6630.
65 B. Ding, C. Hua, C. J. Kepert and D. M. D'Alessandro, *Chem. Sci.*, 2019, **10**, 1392–1400.
66 I. Roy, S. Goswami, R. M. Young, I. Schlesinger, M. R. Mian, A. E. Enciso, X. Zhang, J. E. Hornick, O. K. Farha, M. R. Wasielewski, J. T. Hupp and J. F. Stoddart, *J. Am. Chem. Soc.*, 2021, **143**, 5053–5059.
67 Y.-N. Dong, Z.-K. Liu, J.-P. Xue, Y. Li, K. Sun, Z.-S. Yao and J. Tao, *Inorg. Chem.*, 2022, **61**, 20232–20236.
68 R. F. P. Clementino, A. B. de Souza Santos, O. J. B. J. Marques, D. R. Ratkovski, C. C. Gatto, I. Malvestiti, F. L. de

Araujo Machado and E. H. L. Falcão, *J. Solid State Chem.*, 2018, **268**, 94–101.
69 J. Ying, N. Gao, H. Mou and A. Tian, *J. Solid State Chem.*, 2022, **314**, 123343.
70 T. Liu, H. Cui, X. Zhang, Z.-Y. Zhang, R.-B. Lin, B. Liang, J. Zhang, D. Li and B. Chen, *ACS Appl. Mater. Interfaces*, 2020, **12**, 48712–48717.
71 M.-H. Li, M.-H. You, J.-Y. Zhang, W.-C. Xiao and M.-J. Lin, *CrystEngComm*, 2018, **20**, 7795–7801.
72 Z.-W. Zhai, S.-H. Yang, Y.-R. Lv, C.-X. Du, L.-K. Li and S.-Q. Zang, *Dalton Trans.*, 2019, **48**, 4007–4014.
73 R. Goswami, A. Karmakar, S. Rajput, M. Singh, S. Kundu and S. Neogi, *Mater. Chem. Front.*, 2023, **7**, 881–896.
74 R. Chand, A. Karmakar, S. Kundu and S. Neogi, *Small*, 2024, **20**, 2404085.
75 H.-X. Liu, Z.-J. Zhou, L. Xie, C. Liu, L. Cai, X.-P. Wu and T.-F. Liu, *Angew. Chem., Int. Ed.*, 2024, **63**, e202411508.